

Characterization of internal tide incoherence : Eulerian versus Lagrangian perspectives

Zoé Caspar-Cohen^{1,1}, Aurélien Ponte^{2,2}, Noé Lahaye^{3,3}, Xavier Carton^{4,4}, Xiaolong Yu^{5,5}, and Sylvie Le Gentil^{5,5}

¹LOPS-Ifremer

²LOPS-IFREMER

³Inria & IRMAR, campus universitaire de Beaulieu

⁴Université de Brest

⁵Ifremer

November 30, 2022

Abstract

The Lagrangian and Eulerian surface current signatures of a low-mode internal tide propagating through a turbulent balanced flow are compared in idealized numerical simulations. Lagrangian and Eulerian total (i.e. coherent plus incoherent) tidal amplitudes are found to be similar. Compared to Eulerian diagnostics, the Lagrangian tidal signal is more incoherent with comparable or smaller incoherence timescales and larger incoherent amplitudes. The larger level of incoherence in Lagrangian data is proposed to result from the deformation of Eulerian internal tide signal induced by drifter displacements. Based on the latter hypothesis, a theoretical model successfully predicts Lagrangian autocovariances by relating Lagrangian and Eulerian autocovariances and the properties of the internal tides and jet. These results have implications for the separation of balanced flow and internal tides signals in the sea level data collected by the future Surface Water and Ocean Topography (SWOT) satellite mission.

1 **Characterization of internal tide incoherence : Eulerian versus**
2 **Lagrangian perspectives**

3 Zoé Caspar-Cohen*, Aurélien Ponte

4 *Ifremer, Université de Brest, CNRS, IRD, Laboratoire d'Océanographie Physique et*
5 *Spatiale (LOPS), IUEM, Brest, France*

6 Noé Lahaye

7 *Inria, IRMAR, campus universitaire de Beaulieu, Rennes, France*

8 Xavier Carton, Xiaolong Yu and Sylvie Le Gentil

9 *Ifremer, Université de Brest, CNRS, IRD, Laboratoire d'Océanographie Physique et*
10 *Spatiale (LOPS), IUEM, Brest, France*

11 *Corresponding author: Zoé Caspar-Cohen, zoe.caspar@ifremer.fr

ABSTRACT

12 The Lagrangian and Eulerian surface current signatures of a low-mode internal tide propa-
13 gating through a turbulent balanced flow are compared in idealized numerical simulations.
14 Lagrangian and Eulerian total (i.e. coherent plus incoherent) tidal amplitudes are found to
15 be similar. Compared to Eulerian diagnostics, the Lagrangian tidal signal is more incoher-
16 ent with comparable or smaller incoherence timescales and larger incoherent amplitudes.
17 The larger level of incoherence in Lagrangian data is proposed to result from the defor-
18 mation of Eulerian internal tide signal induced by drifter displacements. Based on the
19 latter hypothesis, a theoretical model successfully predicts Lagrangian autocovariances
20 by relating Lagrangian and Eulerian autocovariances and the properties of the internal
21 tides and jet. These results have implications for the separation of balanced flow and
22 internal tides signals in the sea level data collected by the future Surface Water and Ocean
23 Topography (SWOT) satellite mission.

24 **1. Introduction**

25 The disentangling of internal tides and balanced flow is a key issue for incoming wide-
26 swath altimetric missions such as the SWOT (Surface and Water and Ocean Topography,
27 (Morrow et al. 2019)) and Guanlan (Chen et al. 2019). SWOT will in particular provide
28 instantaneous 2D sea level maps, with an expected horizontal resolution of the order of
29 15–45 km (Wang et al. 2019). With this resolution, internal tides and mesoscale balanced
30 flow will be captured, providing a unique opportunity to study both motions and their
31 interactions. While both motions have distinct time scales, they can have similar length
32 scales (order of tens to hundreds of kilometers) which makes their separation via spatial
33 filtering difficult. The coarse temporal resolution of these instruments (20 day repeat time
34 approximately for SWOT) will also prevent separation by temporal filtering. The resulting
35 difficult disentanglement of internal tides and balanced flow in wide-swath altimetric
36 data is expected to deteriorate the quality of surface velocity estimations via geostrophy
37 (Chelton et al. 2019).

38 Internal tides (or baroclinic tides) are internal waves generated by the barotropic tide
39 when it passes over a topography (Garrett and Kunze 2007). They are initially phase-
40 locked with the tidal forcing and would remain so if they were propagating in a quiescent
41 environment. Such phase-locked internal tide field is commonly referred to as coherent or
42 stationary¹. However, as internal tides travel in a background stratification that varies in
43 time (Buijsman et al. 2017), or pass through a turbulent jet (Ponte and Klein 2015; Dunphy
44 et al. 2017; Savage et al. 2020), they are disturbed and progressively lose their coherence.
45 The fraction of the internal tide that is no longer phase-locked with the tidal forcing and/or
46 of not constant amplitude is the incoherent internal tide, and the mechanisms and typical
47 timescales associated with this loss of coherency remains insufficiently constrained at
48 present days.

¹The term "stationary" is probably more commonly used in literature. However, to avoid any confusion with the concept of stationarity in the context of statistics, we shall use the term "coherent" – and, conversely, "incoherent" – throughout this paper.

49 Internal tides can then be scattered (towards different scales or frequency), e.g. by the
50 corrugated topography, or dissipated close or far from the generation's site (Whalen et al.
51 2020; Savva and Vanneste 2018; Savage et al. 2020). A fraction of the internal tides
52 energy (mainly high modes) dissipates close to their generation's location (Whalen et al.
53 2020) but a significant part travels in the open ocean over potentially great distances – up
54 to thousands of kilometers – with a low-mode vertical structure (Zhao et al. 2016).

55 Several works used altimeter observations to study baroclinic tide including its inco-
56 herent component. Because of their limited temporal sampling compared to internal
57 tides periods, satellite altimetric observations enables the identification of the internal
58 tide signature that remains coherent over a couple of years (Ray and Zaron 2016; Zaron
59 2019). More recently, averaged amplitudes of non-coherent sea level signatures were also
60 obtained (Zaron 2017; Nelson et al. 2019).

61 To overcome limitations of altimeter data, the use of the global drifter program (GDP)
62 dataset has recently been considered (Zaron 2017, 2019). GDP drifter tracks are resolved
63 temporally down to an hour with a horizontal positioning sufficiently accurate in order
64 to capture the signatures of near-inertial waves (Elipot et al. 2010; Sykulski et al. 2016)
65 and tidal motions (Elipot et al. 2016; Yu et al. 2019; Zaron and Elipot 2020). Assuming
66 specific stochastic models for low-frequency and near-inertial motions, Sykulski et al.
67 (2016) designed for example efficient statistical methods in order to fit models parameters
68 to drifter velocity time series.

69 One of the challenges associated with the analysis and interpretation of Lagrangian data
70 is the advection of a drifter by the flow. The data collected by a drifter as it is displaced
71 by the flow may entangle Eulerian spatial and temporal variability and give a distorted
72 perspective of variability as described in the Eulerian frame of reference. LaCasce (2008)
73 reviewed conceptual frameworks that have been developed in order to tackle this issue
74 (Lumpkin et al. 2002; Middleton 1985; Davis 1983, 1985). Two regimes are typically

75 identified: fixed float and frozen turbulence. The prevalence of one regime over the other
76 is determined by the parameter $\alpha = T_E/T_a$, where T_E is the Eulerian evolution timescale
77 of the flow and T_a is the time required for a drifter to travel the Eulerian characteristic
78 spatial scale of the observed fluctuation. T_a is given by L/U , with U the typical advection
79 velocity and L the spatial scale of fluctuations. If $\alpha \ll 1$, the time required for the drifter
80 to travel the length L is greater than the timescale of the fluctuation, T_E . In this case, one
81 can expect an agreement between the Lagrangian and Eulerian timescales. Conversely, if
82 $\alpha \gg 1$, it takes a drifter a time smaller than T_E to travel a distance L , causing a more rapid
83 fluctuation in the Lagrangian perspective. We apply in these paper these ideas to the case
84 of internal tides interacting with a balanced flow.

85 Zaron and Elipot (2020) found a spectral broadening of barotropic tidal peaks in La-
86 grangian data compared to Eulerian ones, due to flow and/or tides spatial inhomogeneity.
87 Such broadening is expected to complicate the extraction of internal tides properties
88 (e.g. overall amplitudes, coherence/non-coherent fractions, incoherent timescales) from
89 lagrangian drifter data, depending on the regions of the ocean and the associated dynamical
90 regime.

91 In order to improve our understanding of this issue, we quantify and compare in this
92 study the internal tide amplitudes and incoherence timescales diagnosed in Eulerian and
93 Lagrangian frames of reference in an idealized configuration. We first present the numer-
94 ical set-up used in this study as well as the statistical models and methods used to estimate
95 internal tide amplitudes and decorrelation timescales. The results are shown in the second
96 part for one simulation at first, and then for several simulations with varying balanced flow
97 intensities. Lastly, we develop a theoretical model to predict Lagrangian autocovariance
98 from Eulerian one and qualitatively validate it against our numerical simulations. The
99 Discussion of the results and Conclusion complete the paper.

100 **2. Numerical simulations and Lagrangian data**

101 *a. Numerical simulations*

102 We performed idealized numerical simulations of an internal tide crossing a balanced
103 flow. The numerical model is the Coastal and Regional Ocean Community model (CROCO
104 and CROCOTOOLS are available at <https://www.croco-ocean.org>) solving the hydrostatic
105 primitive equations. Its configuration follows Ponte et al. (2017) with a zonally periodic
106 rectangular numerical domain (1024 km x 3072 km). The Coriolis frequency follows the
107 beta-plane approximation and is representative of mid-latitudes. A turbulent zonal bal-
108 anced flow crosses the domain at its center along the meridional direction. Numerical
109 simulations are initialized with a baroclinically unstable balanced flow. Relaxation of zon-
110 ally averaged fields towards initial conditions(velocities, temperature, sea level) maintains
111 the turbulence generated by the balanced flow destabilization. Simulations with different
112 balanced flow strength are obtained by modulating the strength of the initial balanced flow
113 or equivalently the latitudinal thermal gradient. After 500 days, relaxation of the zonal
114 mean fields toward the initial balanced flow is ceased. The balanced flow has a mean
115 velocity amplitude maximum around 1450km in the center of the balanced flow (Fig.1a,
116 red line). The balanced flow amplitude decays over the observed period of time with a
117 maximum around 0.6 m/s at the beginning and around 0.4 m/s at the end. The balanced
118 flow velocity is computed by averaging each velocity component (u and v) over 2 days.
119 The balanced flow is surfaced intensified (Fig. 1c) and its vertical structure essentially
120 consists of the barotropic and first baroclinic modes. In the center area, the low-passed
121 velocity indicates ~60% and ~40% of the kinetic energy are found in the barotropic and
122 first baroclinic mode respectively.

123 A mode-1 internal tide is generated at $y = 400$ km with a semi-diurnal frequency (2 cpd).
124 Its signature at the surface dominates the total velocity amplitude in the northern and
125 southern areas (Fig.1a, green line compared to red line). The mode-1 wavelength is

126 approximately between 165 and 185 km. It is worth mentioning that the first baroclinic
127 mode accounts for 98% of the the internal tide's vertically-integrated kinetic energy south
128 and north of the balanced flow and around 90% in the balanced flow. The generation
129 of internal tide higher modes after interaction with the balanced flow is thus negligible
130 in our simulations. Sponge layers at the top and the bottom of the domain ($y < 300$ km
131 and $y > 2700$ km) prevent reflections against top and bottom boundaries. Finally, about
132 8000 simulated near-surface drifters (referred to as drifters in the rest of this study) are
133 also initialized at day 500 on a regular grid extending from 600 km to 2400 km and are
134 advected online (Fig.1b).

135 Dunphy et al. (2017) reports, for the same numerical setup, on the nature of interactions
136 between balanced flow and internal tide and, in particular, on the role played by the respec-
137 tive vertical structures of both processes. This work instead focuses on the distortions of
138 the internal tide signal induced by displacements of surface drifters which explains why
139 most of the attention is paid next on surface flow properties. Further discussion on the
140 relative spatial structures of both processes for this more specific issue are found in section
141 5a.

142 *b. Lagrangian outputs overview*

143 In the central part of the domain, the balanced flow dominates drifter net motions with
144 averaged displacements of about 300 km in the x -direction and 160 km in the y -direction
145 over a 40 day time window (Fig. 2c). For comparison purposes the internal tide wavelength
146 is of about 175km.

147 Away from the balanced flow (Fig.2a and e), the net distance traveled in the y -direction
148 by the selected drifters is of about 20–30 km – which is a fraction of an internal tide
149 wavelength. Internal tides, on the other hand, generate smaller oscillatory displacements,
150 of the order of 2–3 km.

151 Eulerian and Lagrangian meridional velocity time series exhibit significant differences,
 152 visually, in the balanced flow at both low and internal tide frequency (amplitude and
 153 phase) over a 40 day temporal window (Fig. 2d). Meridional velocity time series outside
 154 the balanced flow (Fig. 2b and f) exhibit smaller differences between both frames of
 155 reference. Modulations of internal tide fluctuations are faster in the north compared to the
 156 south in both Eulerian and Lagrangian time series. This discrepancy reflects the loss of
 157 coherence of the internal tide as it propagates northward and interacts with the balanced
 158 flow.

159 *c. Methods : Estimation of Eulerian and Lagrangian amplitudes and timescales*

160 To quantify the loss of coherence of internal tides and the differences and similar-
 161 ities between Eulerian and Lagrangian diagnostics, we estimate amplitude and decorre-
 162 lation/incoherence time scales associated with the balanced flow and internal tides and
 163 compare the results in different parts of the domain.

164 1) AUTOCORRELATION MODELS

165 For both the Eulerian and Lagrangian signals, we assume that a time dependent velocity
 166 component v may be written as the sum of an internal tide part, \tilde{v} , and a balanced (or jet)
 167 part, \bar{v} :

$$v = \tilde{v} + \bar{v} \quad (1)$$

168 where actual spatial and temporal dependencies have been omitted. Note that an alter-
 169 native would be to use a complex velocity, $w = u + iv$ instead of individual components
 170 (zonal or meridional) (Sykulski et al. 2016). This choice is justified when dealing with
 171 polarized motions such as near-inertial waves but is less relevant for internal tides. We
 172 considered that this is not needed in our case and would be more suited for more realistic

173 configurations including inertial waves (Sykulski et al. 2016).

174

175 We assume the internal tide velocity time series is described by :

$$\tilde{v}(t) = \Re \left[\tilde{v}_e(t) e^{i\omega t} \right] \text{ with } \Re \text{ the real part} \quad (2)$$

176 where \tilde{v}_e is the complex-valued amplitude of the tidal oscillations of the tides and depends
 177 slowly on time, thus capturing the incoherence of the tide, and, where $\omega/2\pi$ is the frequency
 178 of the internal tide.

179 The internal tide signal can be decomposed into coherent and incoherent contributions.
 180 The coherent part is defined with a coherent temporal averaging operator, $\langle \cdot \rangle_c$ (i.e. a
 181 temporal average with fixed phased with respect to ω frequency oscillations) :

$$\tilde{v}_{coh} = \langle \tilde{v} \rangle_c, \quad (3)$$

$$= \Re \left[\langle \tilde{v}_e \rangle_c e^{i\omega t} \right] \quad (4)$$

182 where $\langle \cdot \rangle$ is a time averaging operator.

183 Hence the incoherent part, defined as the total velocity minus the coherent part :

$$\tilde{v}_{inc} = \tilde{v} - \langle \tilde{v} \rangle_c, \quad (5)$$

$$= \Re \left[(\tilde{v}_e - \langle \tilde{v}_e \rangle_c) e^{i\omega t} \right] \quad (6)$$

184 Assuming internal tide velocities and jet velocities are uncorrelated, the total autocovari-
 185 ance, C , equals to the sum of the autocovariances of \tilde{v} and \bar{v} :

$$C(\tau) = \langle v(t)v(t+\tau) \rangle = \tilde{C}(\tau) + \bar{C}(\tau), \quad (7)$$

186 There is no report in the literature nor clear physical expectations for the shape of
 187 incoherent signal complex amplitudes. A heuristic choice is thus made here by assuming
 188 the envelope of the internal tide autocovariance is an exponentially decaying function of
 189 time lag, with a decay timescale, \tilde{T} , which will be referred to as the incoherence timescale.

190 The tide autocovariance is expressed as:

$$\tilde{C}(\tau) = \tilde{V}^2 \left[\alpha + (1 - \alpha)e^{-\tau/\tilde{T}} \right] \times \cos(\omega\tau) \quad (8)$$

191 where \tilde{V} and α are constants corresponding to the total tidal amplitude and the coherence
 192 level respectively. The variance of the coherent and incoherent signal are given by $\alpha\tilde{V}^2$
 193 and $(1 - \alpha)\tilde{V}^2$ respectively. This model bears some resemblance with the autocorrelation
 194 derived by Sykulski et al. (2016). We stress however that the resemblance is fortuitous
 195 as the derivation of Sykulski et al. (2016) is not expected to hold for internal tides whose
 196 generation mechanisms and dynamics differ substantially from that of near-inertial waves
 197 which would not justify the use of the same model a priori.

198 The balanced velocity autocovariance is assumed to have the simple form :

$$\bar{C}(\tau) = \bar{V}^2 e^{-\tau/\bar{T}} \quad (9)$$

199 where \bar{T} is the decorrelation timescale. An alternative model was proposed by Veneziani
 200 et al. (2004), introducing a term of balanced flow oscillation, $\cos(\Omega\tau)$, which accounts for
 201 eddies and meanders. The model does improve the visual agreement between meridional
 202 autocorrelations and their fit in the center of the domain but does not affect estimates of
 203 internal tide properties which are the focus of this study. We thus opted for the simpler
 204 form Eq.9.

205 The total autocovariance is finally given by:

$$C(\tau) = \tilde{C}(\tau) + \bar{C}(\tau) = \tilde{V}^2 \left[\alpha + (1 - \alpha)e^{-\tau/\tilde{T}} \right] \times \cos(\omega\tau) + \bar{V}^2 e^{-\tau/\bar{T}} \quad (10)$$

206 2) AUTOCORRELATIONS AND PARAMETERS ESTIMATION

207 For each drifter's trajectory the velocity time series is split into segments of length
 208 T_w , overlapping each other by 50%. A time window of 40 day is chosen. This value
 209 is the result of the following compromise: time windows used for the computation of
 210 Lagrangian individual autocovariances has to be short enough for the result to be typical

211 of a specific area, while being long enough to capture potentially long decorrelation
212 timescales. Eulerian mean velocities, averaged in time and zonal direction is interpolated
213 on drifters trajectories and removed. No significant impacts of this removal were observed
214 on the results for the tidal signal. Individual autocovariances are then computed over
215 each segment and averaged within 50 km wide meridional bins. Each autocovariance
216 segment is attributed to a bin depending on the mean position over the period T. We
217 did not find a significant sensitivity of our results to the length of the window. The
218 Eulerian individual autocovariance is computed at each grid point using the same time
219 windows and bin-averaged meridionally as for the Lagrangian autocovariance. Averaged
220 autocovariances are then divided by the averaged autocovariance at time lag zero to obtain
221 the averaged autocorrelation.

222

223 The heuristic model, developed in section2c1, is fitted to averaged autocovariances
224 which provides estimates for parameters \tilde{T} , \tilde{V}^2, α , \bar{T} and \bar{V}^2 to find the best fit. The fit is
225 done using a non linear least square regression (Jones et al. 2001–). Lower bounds are
226 fixed to zero for amplitudes and one and two days for \tilde{T} and \bar{T} respectively. Confidence
227 intervals are computed using a bootstrap method (Efron 1981). Within each bin, individual
228 autocovariances are randomly resampled one hundred times (with replacement). Each
229 resampled dataset leads to an averaged autocovariance and amplitudes and timescales
230 parameters estimates using the fit described previously. 95% confidence intervals are
231 derived from the distribution of the parameter estimates.

232 **3. Signatures of internal tides and balanced flow in Eulerian and Lagrangian per-** 233 **spective**

234 *a. Velocity autocorrelations*

235 Lagrangian and Eulerian velocity autocorrelations (resp. Fig. 3 a and b; function of time
236 lag and y) highlight three regimes that coincides with the southern ($y < 1000\text{km}$), central
237 ($1000\text{km} < y < 1800\text{km}$), and, northern ($y > 1800\text{km}$) parts of the numerical domain and
238 correspond to typical drifter trajectories shown in Fig. 2a, c and e.

239 Autocorrelation at these latitudes of interest are further shown in Fig. 4.

240 In the northern and southern parts of the numerical domain, semi-diurnal oscillations
241 associated with internal tides, stand out on both Eulerian and Lagrangian autocorrelations.
242 In these areas, the signal seems to be dominated by internal tides with no signature of the
243 balanced flow visually. No decay of oscillations amplitudes with time lag are visible in
244 the south —especially in the Eulerian perspective (see Fig. 4f)— indicating that internal
245 tides are nearly coherent there. A mild decay of these oscillations is observed in the north,
246 on the other hand, and indicates internal tides are partially incoherent there. There are
247 no significant visual differences between Lagrangian and Eulerian autocorrelations in the
248 northern and southern areas.

249 Conversely, the central area exhibits a decay – especially in the Lagrangian perspective
250 – of the tidal oscillations combined to a slower general decay associated with the slower
251 balanced motion. As observed in drifters trajectories and velocity time series (Fig. 2, panels
252 c and d), this is the area where drifters are most significantly displaced by the balanced
253 flow and where Lagrangian and Eulerian time series differ substantially. Semi-diurnal
254 oscillations of the Lagrangian autocorrelation are not visible after lags of about 5 days
255 (Fig. 3a and Fig. 4c) while they are observed after 20 days on the Eulerian autocorrelation
256 (Fig. 3b and Fig. 4d). The decorrelation of the balanced motion is also faster in Lagrangian

257 autocorrelation compared to Eulerian one, and exhibits a negative lobe around $\tau \sim 4$ days
258 which we attribute to the meridionally oscillating trajectories of drifters caught in the
259 balanced flow.

260 The faster decay of the low-frequency signature on Lagrangian autocorrelations is at-
261 tributed to the projection of spatial variability into temporal one along drifter trajectories
262 (Lumpkin et al. 2002; LaCasce 2008).

263 *b. Estimates of velocity amplitudes and decorrelation timescales*

264 Eulerian meridional profiles of incoherence timescales and coherent and incoherent tide
265 amplitudes (blue lines Fig.5a, c and d) obtained after fitting averaged autocovariances onto
266 Eq.10 translate a loss of the coherence of internal tides during the crossing of the balanced
267 flow. In the south, the tidal signal is essentially coherent with Eulerian coherence level
268 close to 1; see Fig. 5c) and a flat envelope of autocorrelations oscillations (Fig. 4f).

269 In the center of the numerical domain, the internal tide propagation is perturbed by the
270 balanced flow and results in a loss of coherence with a decrease of the coherence level. This
271 trend culminates in the northern part of the domain with a ratio of coherent variance over
272 total tidal variance between 0.2 and 0.4. Note that the total (coherent+incoherent) tidal
273 variance increases northward (Fig. 5d). This increase is caused by variations of the Coriolis
274 frequency and of the stratification. Furthermore, a northwards surface intensification of the
275 vertical mode structure requires an increase of the surface amplitude for a given vertically
276 integrated energy flux. All together, these mechanisms result in a northward increase of
277 the surface amplitudes of internal tide.

278 Incoherent timescales exhibit values of about 5 days in the south and increases northward
279 to reach values comprised between 10 and 20 days. We note that the envelope of the
280 Eulerian tidal oscillations in the north (blue lines Fig. 4b) does reach a plateau, consistent

281 with a remaining coherent component and justifying the form of the fit for the motions we
282 use (eq. 8).

283 Lagrangian parameters present a significantly different picture compared to Eulerian
284 ones as suggested by drifter trajectories (Fig. 2 a, c and e) and autocorrelations (Fig. 3).
285 In the south, the envelope of the Lagrangian autocorrelation (Fig. 4 e) decays faster than
286 the Eulerian one. Lagrangian coherence levels (red lines on Fig. 5c) range from 0.0 to 0.7.
287 Incoherent timescales (Fig. 5a) remain between 10 and 20 days. In the center, Lagrangian
288 tidal variance is largely incoherent with α_L close to zero. Incoherent timescales decrease
289 sharply in the same area down to 1 day in its center. We coin "apparent incoherence" the
290 larger level of incoherence (i.e. smaller incoherence timescales, \tilde{T} and coherence level α)
291 of internal tide signature on Lagrangian velocities compared to Eulerian one and attribute
292 it to the distortion of the Eulerian signal by balanced motions which is largest in the center
293 area. In the north, such apparent incoherence diminishes and Lagrangian autocorrelations
294 and parameters are comparable to Eulerian ones (Fig. 4 a and b, Fig. 5a and c). Regardless
295 of this apparent incoherence, the total tidal variance is found similar in both Lagrangian
296 and Eulerian autocorrelations (Fig. 5d).

297 As expected, balanced motions variances diagnosed from autocorrelations parametric
298 fit are maximum in the central area where the balanced flow resides (Fig. 5e). The
299 Lagrangian balanced motion decorrelation timescales (Fig. 5b) reach the lowest boundary
300 (~ 2 days) in the central area. The Eulerian decorrelation timescales are larger, ≤ 10 days.
301 It corresponds to the area of high balanced amplitude (Fig. 5e). It also coincides with the
302 area of low Lagrangian incoherence timescales which supports an apparent incoherence
303 in Lagrangian diagnostics dominant in this part.

304 *c. Sensitivity to the balanced flow EKE*

305 The sensitivity of internal tide Lagrangian/Eulerian properties to the balanced flow
306 EKE is investigated with five numerical simulations of increasing balanced flow strength.
307 The meridional distributions of velocity amplitudes indicates a two-fold increase across
308 simulations (Fig.6b).

309 The internal tide total velocity variance \tilde{V}^2 increases northwards (Fig.6d), as explained
310 in section 3b. This increase is more pronounced for larger balanced flow strength, as
311 expected from the larger change of stratification, and is of similar magnitude in both
312 Eulerian and Lagrangian perspectives.

313 Starting with the two most energetic simulations, S_3 and S_4 , both Eulerian and La-
314 grangian diagnostics show a loss of coherence of internal tides that occurs when internal
315 tides cross the balanced flow. In the south area, the Eulerian coherence level is around 1,
316 which indicates the internal tide is essentially coherent there (dashed lines in Fig. 6c). La-
317 grangian coherence level, on the other hand, decreases rapidly below 0.1 which indicates
318 substantial apparent incoherence.

319 In the center area, Eulerian coherence level decreases towards 0.6 while the Lagrangian
320 one remains below 0.1. Lagrangian incoherent timescales (Fig. 6a) reach minimal values
321 (≤ 5 days) while Eulerian ones remain around or above 5 days in all simulations. The
322 width of this area of apparent incoherence is clearly identified from Lagrangian incoherent
323 timescales (Fig. 6a) and is consistent with the increase of the strength of the balanced flow
324 (Fig. 6b).

325 In the northern area, both simulations exhibit comparable Eulerian and Lagrangian
326 coherence level and incoherence timescales, i.e. there is little apparent incoherence.

327 In the intermediate case, S_2 , a sharp decrease of Lagrangian coherence level points
328 towards apparent incoherence in the center area similarly to S_3 and S_4 . The Eulerian
329 coherence level drops sharply to 0 in the north while the incoherent timescale increases

330 towards values between 30 and 40 days unlike S_3 and S_4 . This discrepancy might result
 331 from an inconsistent behaviour of the fit associated with an absence of plateau in Eulerian
 332 autocorrelations and the ambiguous distinction between coherent and slowly incoherent
 333 signals in such situation.

334 Unlike S_3 and S_4 the two least energetic simulations, S_0 and S_1 , exhibit a weak loss
 335 of coherence in Eulerian perspective as coherence levels are above 0.6 at all meridional
 336 positions. Lagrangian coherence level drops sharply to zero in the balanced flow while
 337 incoherence timescales drop to 1 day. This indicates that Lagrangian apparent incoherence
 338 is effective even in weakly energetic simulations.

339 **4. Lagrangian model for autocovariance and comparison to observed autocovariance**

340 *a. Theoretical expectation for the Lagrangian autocorrelation*

341 A theoretical model is developed next in order to predict Lagrangian velocity auto-
 342 covariances based on Eulerian ones along with flow parameters. The model effectively
 343 represents distortions, in the Lagrangian frame of reference, of Eulerian tidal fluctuations
 344 induced by drifters displacements associated with the balanced flow.

345 We then validate this model based on the Eulerian and Lagrangian autocovariance
 346 presented in previous sections.

347 We assume that the tidal signal is a modulated monochromatic wave propagating in a
 348 single direction (say x) and characterized by a frequency ω and wavenumber k :

$$\tilde{v}(x, t) = \Re \left\{ \tilde{v}_e(x, t) e^{i(\omega t - kx)} \right\}, \quad (11)$$

349 where \tilde{v}_e is the complex amplitude, which varies slowly both in time and space. Let's
 350 consider a parcel traveling with the flow with trajectory $X(t)$. The autocovariance of \tilde{v} as

351 measured along the parcel trajectory is given by:

$$\tilde{C}_L(\tau) = \langle \tilde{v}(t+\tau)\tilde{v}(t) \rangle, \quad (12)$$

$$= \frac{1}{2} \Re \left\{ \left\langle \tilde{v}_e [X(t+\tau), t+\tau] \tilde{v}_e^* [X(t), t] e^{i[\omega\tau - k(X(t+\tau) - X(t))]} \right\rangle \right\}, \quad (13)$$

$$= \frac{1}{2} \Re \left\{ e^{i\omega\tau} \times \left\langle \tilde{v}_e [X(t+\tau), t+\tau] \tilde{v}_e^* [X(t), t] e^{-ik\delta X(t,\tau)} \right\rangle \right\}, \quad (14)$$

352 where we assume that oscillation terms ($\propto e^{\pm 2i\omega t}$) are smoothed out by the averaging
 353 procedure and we have introduced the displacement $\delta X(t, \tau) = X(t + \tau) - X(t)$.

354 We assume here that the internal tide is not transported by the balanced surface flow
 355 which is reasonable for low mode internal tides as further discussed in section 5a. In such
 356 case, the amplitude of the tide and the displacement are presumably uncorrelated:

$$\tilde{C}_L(\tau) = \frac{1}{2} \Re \left\{ e^{i\omega\tau} \times \left\langle \tilde{v}_e [X(t+\tau), t+\tau] \tilde{v}_e^* [X(t), t] \right\rangle \times \left\langle e^{-ik\delta X(t,\tau)} \right\rangle \right\}, \quad (15)$$

357 The second term in the product of (15) right hand-side combines both the spatial and
 358 temporal variability of the Eulerian tidal envelope in general. As further discussed in
 359 sect. 4b, horizontal displacements after time intervals comparable to a incoherent time
 360 scale can be expected to be smaller than the length scale of the complex amplitude of the
 361 tide, which leads to:

$$\left\langle \tilde{v}_e [X(t+\tau), t+\tau] \tilde{v}_e^* [X(t), t] \right\rangle \approx \tilde{C}_e(\tau), \quad (16)$$

362 where $\tilde{C}_e(\tau)$ is the fixed point (i.e. zero spatial lag) autocovariance of the tidal amplitude.

363 The displacement may be decomposed into a wave high frequency contribution and
 364 a lower frequency component that may be associated with an independent flow and/or
 365 wave motions themselves via second order effects (Wagner and Young 2015). The former
 366 contribution is time periodic with frequency ω and a bounded amplitude equal to the wave
 367 excursion (\tilde{V}/ω where \tilde{V} is the amplitude of the wave velocity) which is small compared to
 368 $1/k$ (0.4-0.7 versus 25-35 km/rad for our simulations). The low frequency displacement is

369 likely to continuously grow on the other hand and produces a displacement that ultimately
370 dominates in the exponential of (15) right hand-side third term, even for flow amplitudes
371 smaller than tidal ones. We will thus ignore tide displacements in the latter exponential.
372 To proceed further, we assume that the balanced flow is a stationary Gaussian process,
373 with rms amplitude \bar{V} (over one direction) and exponential decorrelation in time with
374 typical time scale \bar{T} – consistently with the model (9).

375 Such model – sometimes referred as an unbiased correlated velocity model in the liter-
376 ature (Gurarie et al. 2017) – corresponds to the time-homogeneous Ornstein-Uhlenbeck
377 process. The displacement $\delta X(t, \tau)$ is also a Gaussian process with null mean and variance
378 given by (Pope 2015, Chap. 12):

$$\sigma^2(\tau) \equiv \langle \delta X(t, \tau)^2 \rangle = 2\bar{T}^2\bar{V}^2 \left[\tau/\bar{T} - \left(1 - e^{-\tau/\bar{T}}\right) \right]. \quad (17)$$

379 Note that the variance of the displacement admits two asymptotic regimes : $\sigma^2(\tau) \rightarrow \bar{V}^2\tau^2$
380 for $\tau \ll \bar{T}$, and $\sigma^2(\tau) \rightarrow 2\bar{V}^2\bar{T}\tau$ for $\tau \gg \bar{T}$. The third term in the right hand side of eq. (15)
381 may then be computed :

$$\left\langle e^{-ik\delta X(t, \tau)} \right\rangle = \int_{-\infty}^{\infty} \cos(k\delta X) p(\delta X) d\delta X, \quad (18)$$

$$= \int_{-\infty}^{\infty} \cos(k\delta X) \frac{e^{-\delta X^2/(2\sigma^2)}}{\sigma\sqrt{2\pi}} d\delta X \quad (19)$$

$$= e^{-\sigma^2 k^2/2} = \exp\left(-k^2\bar{V}^2\bar{T}^2 \left[\tau/\bar{T} - (1 - e^{-\tau/\bar{T}}) \right]\right) \quad (20)$$

382 Combining (16) with (20) into (15) leads to the following expression for the autocovari-
383 ance of internal tide in the Lagrangian frame of reference:

$$\tilde{C}_L(\tau) = \tilde{C}_e(\tau) \cos(\omega\tau) e^{-\sigma^2(\tau)k^2/2} \quad (21)$$

$$= \tilde{C}_E(\tau) e^{-\sigma^2(\tau)k^2/2}, \quad (22)$$

384 which becomes with the heuristic model of Eulerian tidal autocovariance \tilde{C}_E Eq.(8):

$$\tilde{C}_L(\tau) = \cos(\omega\tau) \tilde{V}^2 \left(\alpha + (1 - \alpha) \exp(-\tau/\tilde{T}_E) \right) e^{-\sigma^2(\tau)k^2/2} \quad (23)$$

385 The Lagrangian autocorrelation Eq.(22) and Eq.(23) has no coherent part and decays
 386 as fast or faster than the Eulerian autocorrelation because of the last term on the right
 387 hand-side of both equations. This larger incoherence in the Lagrangian frame of reference
 388 embodies the "apparent incoherence". Its origin is purely kinematic and associated with
 389 drifter displacements relative to tidal phase patterns as indicated by the origin of this term
 390 in (15). We define the "apparent incoherence timescale" as the timescale \tilde{T}_{app} that satisfies:

$$k^2 \sigma^2 (\tilde{T}_{app}) = 1 \quad (24)$$

391 Figure 7 summarizes the different regimes of coherence/incoherence encountered with
 392 the present theoretical model. In the Eulerian frame of reference, tidal autocorrelations
 393 are controlled by the coherence level α_E . For moderate to low α_E , the autocorrelation
 394 decays over the timescale \tilde{T}_E to a plateau (zero) in moderately (low) coherent cases. In the
 395 Lagrangian frame of reference, the shape of the tidal autocorrelation is first determined
 396 by the relative size of the Eulerian incoherence timescale compared to the apparent one:

- 397 • When the Eulerian incoherence timescale is larger than the apparent one ($\tilde{T}_E \gg \tilde{T}_{app}$),
 398 advection by the slow flow is strong enough for apparent incoherence to control the
 399 Lagrangian tidal autocorrelation. The shape of the Lagrangian autocorrelation is
 400 either gaussian for long balanced flow autocorrelation timescales ($k\bar{VT} \gg 1$) (Fig. 7,
 401 label (2)) with incoherence timescale $(k\bar{V})^{-1}$ or exponential for short balanced flow
 402 autocorrelation timescales ($k\bar{VT} \ll 1$) with incoherence timescale $(k\bar{V})^{-1} \times (k\bar{VT})^{-1}$.
- 403 • When the Eulerian incoherence timescale is smaller than the apparent one ($\tilde{T}_E \ll$
 404 \tilde{T}_{app}), the Eulerian level of incoherence determines the shape of the Lagrangian
 405 tidal autocorrelation. In coherent situations ($\alpha \sim 1$), Lagrangian autocorrelations are
 406 controlled by apparent incoherence with an exponential or gaussian shape depending
 407 on the size of the balanced flow autocorrelation timescale (via the non-dimensional
 408 parameter $k\bar{VT}$) (Fig. 7, label (1)) as for $\tilde{T}_E \gg \tilde{T}_{app}$. For intermediate Eulerian

409 coherence levels ($0 < \alpha < 1$), the Lagrangian autocorrelation exhibits a first decay
410 over the Eulerian incoherence timescale \tilde{T}_E and a second, slower decay at the apparent
411 incoherence timescale \tilde{T}_{app} (Fig. 7, label (3)). For low levels of Eulerian coherence,
412 the Lagrangian autocorrelation is solely controlled by the Eulerian one with no effect
413 of apparent incoherence.

414 *b. Comparison of observed autocovariances and predicted Lagrangian ones*

415 Observed Lagrangian internal tide autocorrelation envelopes (Fig. 8 middle column)
416 are assembled from Lagrangian averaged autocovariance fitted parameters and Eq.8 (with
417 the cosine term omitted and normalization by the value at lag 0). These envelopes
418 are compared to predicted Lagrangian envelopes (Fig. 8 right column) estimated from
419 observed Eulerian autocovariances (assembled similarly as Lagrangian ones and shown
420 on Fig. 8 left column) and Eq. (22)

421 Observed Eulerian autocorrelation envelopes exhibit decay rates that are increasingly
422 faster in the northwards direction for all three simulations considered (S_0 , S_2 and S_4 ; shown
423 in Fig. 8, top, middle and bottom rows respectively). This reflects the loss of coherence
424 of the internal tide as it propagates northwards.

425 Observed Lagrangian autocorrelation envelopes have markedly different structure with
426 a well-defined central area characterized by a rapid (couple of days timescale) fall-off
427 compared to Eulerian envelopes. The width of this area of strong apparent incoherence
428 is increasing with the balanced flow strength. Outside of this area, the south and north
429 autocorrelation decay are slower and hence closer to Eulerian ones with a more rapid
430 decay in the north compared to the south. Predicted Lagrangian envelopes reproduce the
431 rapid envelope fall-off in the center, the north/south contrast, as well as the sensitivity of
432 the envelopes to balanced flow strength. We conclude the model proposed in order to
433 relate Eulerian and Lagrangian tidal autocovariances is thus consistent with observations.

434 The Eulerian coherence level, α (dashed lines Fig. 6c), and the ratio between the Eulerian
435 incoherence timescale and the apparent incoherence timescale (Fig. 9a) provide all the
436 necessary information to interpret and predict the nature of Lagrangian incoherence. Its
437 form is controlled by the parameter $k\overline{VT}$ (Fig. 9c).

438 In the southern area, the Eulerian coherence level is around 1 for all simulations: internal
439 tides are coherent in the Eulerian frame of reference. Eulerian incoherence timescales are
440 smaller than \tilde{T}_{app} . Lagrangian autocorrelations are controlled by $k\overline{VT}$ which is lower than
441 one in the area, suggesting an expected exponentially decaying form. Observed Lagrangian
442 incoherence timescales are moderately weaker than their theoretical predictions \tilde{T}_{app} with
443 values of their ratio between 0.2 and 0.7 (Fig. 9b).

444 In the central area, the Eulerian coherence level is moderate (e.g. between 0.4 and 0.9)
445 and the Lagrangian one close to zero. Eulerian incoherence timescales are larger than
446 apparent incoherence timescales (ratio up to 20 for least energetic simulations). Observed
447 Lagrangian incoherence timescales are also close to their theoretical predictions. This
448 regime corresponds to the first regime described in section 4a and Fig. 7(label (2)) of
449 strong apparent incoherence. $k\overline{VT}$ is larger than one which would be associated with
450 a gaussian autocorrelation envelope and an apparent incoherence insensitive to the slow
451 flow time-variability.

452 In the north, Eulerian coherence levels, α_E , remain moderate (ranges from 0.2-0.3 for
453 S_3 and S_4 to 0.6-0.8 for S_0 and S_1), there is some Eulerian incoherence or even prevalence
454 of the incoherent signal for S_3 and S_4 . Eulerian incoherence timescales is smaller than
455 apparent incoherence timescales. We interpret this regime (section 4a and Fig. 7 label
456 (3)) as one where the observed Lagrangian incoherence is dominated by the Eulerian
457 incoherence, while being moderately affected by the Lagrangian distortion.

458 5. Discussion

459 a. On the nature of internal tide propagation in the presence of a background flow

460 The assumption of no transport of the internal tide by the surface flow used to derive
461 (15) is now discussed. Low mode internal tides have by definition large vertical scales –
462 similar to that of the background flow. Advection by the balanced flow is of particular
463 importance for discussing the Eulerian/Lagrangian distortion, even though it does not
464 fully capture the interaction between the balanced flow and the internal tide (Dunphy et al.
465 2017; Savage et al. 2020). A vertical mode expansion of equations of motions linearized
466 around the balanced background flow shows that advection of the internal tide mode is
467 driven by a non-trivial weighted average of the background flow. This effective advection
468 is expressed as $H^{-1} \int_{-H}^0 \phi_n^2 \mathbf{U} dz$ (Kelly and Lermusiaux 2016), where ϕ_n is the standard
469 pressure mode for an internal tide with vertical mode number n and \mathbf{U} is the balanced flow
470 (see also Duda et al. 2018, for a more technical approach). Thus, for a surface intensified
471 background flow, the flow advecting the drifter (at the surface) and the one advecting the
472 internal tide mode is different, explaining why the Lagrangian observer renders a distorted
473 view of the internal tide signal. For the simulation with moderate jet intensity S2, for
474 instance, the mode 1 effective advection velocity (computed, but not shown) is of order
475 0.2 ms^{-1} at its maximum, while the surface velocity is typically greater than 1 ms^{-1} : the
476 Eulerian distortion, driven by the effective advection velocity, is therefore smaller than the
477 Lagrangian distortion, driven by the difference between this effective advection and the
478 surface velocity transporting the drifter.

479 For small scale internal tides on the other hand, ray theory can be used to describe
480 their propagation through the background flow (Broutman et al. 2004). This approach
481 shows that wave packets are advected by the local flow, which is associated with a Doppler
482 shifting of the Eulerian frequency: $\omega = \hat{\omega} + \mathbf{k} \cdot \mathbf{U}$, where ω and $\hat{\omega}$ are respectively the
483 tide absolute (or Eulerian) and intrinsic (as measured in a frame of reference moving

484 with the balanced flow) frequencies and \mathbf{k} is the wave vector. Ignoring advection of the
 485 drifter by the tidal current, the signal measured by the drifter coincides with the tidal
 486 field in the frame co-moving with the mean flow with least distortion in the Lagrangian
 487 frame of reference. This situation is opposite to the configuration investigated here, as
 488 Lagrangian autocorrelation exhibits faster decrease with time lag compared to Eulerian
 489 auto-correlation, and the theoretical model proposed here would obviously not be relevant.

490 In a realistic configuration, the range of validity of each of these two regimes (e.g. small
 491 vs large scale internal tide) remains to be quantified.

492 *b. On the internal tide spatial incoherence*

493 Another assumption of the theoretical model required to derive (16) is that spatial vari-
 494 ations of the complex tidal amplitude may be neglected. In reality the amplitude of the
 495 internal tide propagates with the internal tide group speed, which results in spatial variabil-
 496 ity if a temporal one is admitted. A reasonable estimate of the associated horizontal length
 497 scale is $\tilde{T}_E c_g$. A sufficient condition for (16) to hold is thus that the drifter displacement
 498 after a decorrelation time scale \tilde{T}_L remains smaller than the complex amplitude horizontal
 499 length scale:

$$\delta X(\tilde{T}_L) \ll \tilde{T}_E c_g. \quad (25)$$

500 An upper bound for this displacement is $\tilde{T}_L \max(\bar{V}, \tilde{V})$, which enables to rewrite the
 501 preceding condition as:

$$\frac{\tilde{T}_L}{\tilde{T}_E} \ll \frac{c_g}{\max(\bar{V}, \tilde{V})}. \quad (26)$$

502 We believe this condition is met in general based on 1/ typical values for c_g (around
 503 2 m/s for the first mode semi-diurnal internal tide at mid-latitude (Zhao 2017)) and
 504 flow amplitude, 2/ observations that $\tilde{T}_L \leq \tilde{T}_E$, this inequality being self-consistent with
 505 theoretical model predictions and 3/ the observation that stronger flows and thus weaker
 506 c_g/\bar{V} concur with smaller \tilde{T}_L/\tilde{T}_E ratios.

507 Spatial inhomogeneities of the tidal amplitude could, at the cost of added complexity,
508 potentially be included in the model without the approximation (16). This would require
509 combining information about horizontal displacement distribution and the tidal amplitude
510 spatial-temporal autocorrelation. However, diagnostics of spatio-temporal autocorrelation
511 of the internal tide field have never been reported – to our knowledge.

512 *c. Autocorrelation models and coherent/incoherent decomposition*

513 Heuristic choices have been made regarding the shape of the internal tide and balanced
514 motion autocorrelation. Limits to these choices are visible on Figure 4c for balanced
515 motions and are speculated to affect estimates of internal tide incoherent time scales in
516 the southern part of the domain.

517 At earlier stage of this work, we chose an envelope for the internal tide autocorrelation
518 that included a single exponential decaying term instead of the sum of coherent/incoherent
519 contributions. We eventually abandoned this choice, because it does not naturally lead
520 to a decomposition of the signal into coherent/non-coherent contributions, and because
521 it resulted in overly large time scales in coherent cases (>1000 days). One may also fit
522 the more general form Eq.(23) to Lagrangian autocorrelations, for example, and evaluate
523 its relevance compared to the single linear exponential form. This would add one more
524 parameter to estimate, however, and would require to determine whether this more general
525 form leads to a significant an improvement which we felt was a study on its own. Therefore,
526 we did not attempt to do this in favor of a more qualitative assessment of the theory.

527 Determining what form is more appropriate for Eulerian/Lagrangian low-
528 frequency/internal tide autocorrelations is a study on its own that will require more
529 advanced statistical tools (Sykulski et al. 2016; Gurarie et al. 2017) and that we be-
530 lieve may be more relevant to perform in realistic settings (e.g. observation or numerical

531 simulations). Sykulski et al. (2016) proposes a more general alternative with the Matérn
532 process which may help to more accurately modeling statistically the low frequency signal.

533 **6. Conclusion**

534 This study investigated, in idealized numerical simulations, the signature of internal
535 tides on surface velocities via the computation of averaged autocorrelations and fits of
536 these autocorrelations on heuristic models. This exercise was performed on both Eulerian
537 and Lagrangian time series which enabled to compare and contrast internal tide signatures
538 in both frames of reference. The central result of this study is that displacements of drifters
539 induced by low-frequency motions produce distortions of the tide signals in Lagrangian
540 time series which results in larger levels of incoherence compared to Eulerian ones. We
541 coined this process "apparent incoherence". Sensitivity experiments enabled to verify
542 that this apparent incoherence is increasing with balanced-motion intensity. A theoretical
543 model, relating Lagrangian averaged autocovariances to Eulerian ones and accounting for
544 apparent incoherence, was derived and validated against observed estimates.

545 These results highlight the relevance of GDP data for the mapping of global internal tide
546 properties. More specifically, we were able to recover the total internal tide variance from
547 drifter velocity averaged autocorrelations. Pending validation in more realistic conditions,
548 the knowledge of the distribution of internal tide surface kinetic energy that could be
549 inferred from drifter tracks would be a substantial constraint for the mapping of internal
550 tides. Our study suggests that the identification of (Eulerian) coherent versus incoherent
551 contributions from drifter data may be complicated because of apparent incoherence, as
552 anticipated in earlier studies (Zaron and Elipot 2020). This may still be feasible in areas
553 where incoherence is significant and rapid and/or where low-frequency variability is weak.
554 The theoretical model developed may provide guidance in order to decide where this may
555 occur in the ocean. Improved mapping of internal tides are directly relevant to the future

556 analysis of SWOT data, to the validation of emerging high resolution global numerical
557 simulations resolving tides (Arbic et al. 2018; Yu et al. 2019), as well as to our fundamental
558 understanding of internal tide lifecycle.

559 More advanced and likely efficient statistical tools may be required before tackling
560 realistic configurations. Substantial difficulties are associated with the superposition of
561 motions in the real ocean (neighboring tidal harmonics, near-inertial variability) and with
562 the effective statistical stationarity of these motions. Parametric estimations based on
563 maximum likelihood theory offer promising perspectives whether formulated in spectral
564 space (Sykulski et al. 2019) or temporal space (Fleming et al. 2014). Filtering based
565 approaches taking into account the bivariate nature of the velocity signal may also be
566 relevant (Lilly and Olhede 2009). These tools may help identify which statistical models
567 are better suited to describe tidal and low-frequency variability as well as resolve the
568 temporal evolution of the parameters (e.g. amplitude, frequency, bandwidths) describing
569 these processes, which would be a substantial improvement over descriptions of the
570 averaged variability.

571 The estimation of internal tides properties in a realistic set-up will be carried out
572 using MITgcm simulation LLC4320 using Eulerian outputs of the simulation as well as
573 Lagrangian simulated trajectories. Further analysis should enable us to estimate if our
574 results hold in realistic configuration.

575 **References**

576 Arbic, B. K., and Coauthors, 2018: Primer on global internal tide and internal gravity wave
577 continuum modeling in hycom and mitgcm. *New frontiers in operational oceanography*,
578 307–392.

579 Broutman, D., J. W. Rottman, and S. D. Eckermann, 2004: Ray Methods for Internal
580 Waves in the Atmosphere and Ocean. *JGR*.

581 Buijsman, M. C., B. K. Arbic, J. G. Richman, J. F. Shriver, A. J. Wallcraft, and L. Zamudio,
582 2017: Semidiurnal internal tide incoherence in the equatorial Pacific. *Journal of*
583 *Geophysical Research: Oceans*, **122** (7), 5286–5305.

584 Chelton, D. B., M. G. Schlax, R. M. Samelson, J. T. Farrar, M. J. Molemaker, J. C.
585 McWilliams, and J. Gula, 2019: Prospects for future satellite estimation of small-scale
586 variability of ocean surface velocity and vorticity. *Progress in Oceanography*, **173**,
587 256–350.

588 Chen, G., and Coauthors, 2019: Concept design of the “guanlan” science mission: China’s
589 novel contribution to space oceanography. *Frontiers in Marine Science*, **6**, 194.

590 Davis, R., 1983: Oceanic property transport, lagrangian particle statistics, and their
591 prediction. *Journal of Marine Research*, **41** (1), 163–194.

592 Davis, R. E., 1985: Drifter observations of coastal surface currents during CODE: The
593 method and descriptive view. *J. Geophys. Res.*, **90**(C3), 4741–4755.

594 Duda, T. F., Y.-T. Lin, M. Buijsman, and A. E. Newhall, 2018: Internal Tidal Modal
595 Ray Refraction and Energy Ducting in Baroclinic Gulf Stream Currents. *JPO*, **48** (9),
596 1969–1993, doi:10.1175/JPO-D-18-0031.1.

597 Dunphy, M., A. L. Ponte, P. Klein, and S. Le Gentil, 2017: Low-mode internal tide
598 propagation in a turbulent eddy field. *Journal of Physical Oceanography*, **47** (3), 649–
599 665.

600 Efron, B., 1981: Censored data and the bootstrap. *Journal of the American Statistical*
601 *Association*, **76** (374), 312–319.

602 Elipot, S., R. Lumpkin, R. C. Perez, J. M. Lilly, J. J. Early, and A. M. Sykulski, 2016: A
603 global surface drifter data set at hourly resolution. *Journal of Geophysical Research:*
604 *Oceans*, **121** (5), 2937–2966.

- 605 Elipot, S., R. Lumpkin, and G. Prieto, 2010: Modification of inertial oscillations by the
606 mesoscale eddy field. *Journal of Geophysical Research: Oceans*, **115** (C9).
- 607 Fleming, C. H., J. M. Calabrese, T. Mueller, K. A. Olson, P. Leimgruber, and W. F. Fagan,
608 2014: Non-markovian maximum likelihood estimation of autocorrelated movement
609 processes. *Methods in Ecology and Evolution*, **5** (5), 462–472.
- 610 Garrett, C., and E. Kunze, 2007: Internal tide generation in the deep ocean. *Annu. Rev.*
611 *Fluid Mech.*, **39**, 57–87.
- 612 Gurarie, E., C. H. Fleming, W. F. Fagan, K. L. Laidre, J. Hernández-Pliego, and
613 O. Ovaskainen, 2017: Correlated velocity models as a fundamental unit of an-
614 imal movement: Synthesis and applications. *Movement Ecology*, **5** (1), 13, doi:
615 10.1186/s40462-017-0103-3.
- 616 Jones, E., T. Oliphant, P. Peterson, and Coauthors, 2001–: SciPy: Open source scientific
617 tools for Python: Least square regression. [Available online at [https://docs.scipy.org/
618 doc/scipy/reference/generated/scipy.optimize.curve_fit.html](https://docs.scipy.org/doc/scipy/reference/generated/scipy.optimize.curve_fit.html)].
- 619 Kelly, S. M., and P. F. J. Lermusiaux, 2016: Internal-tide interactions with the Gulf
620 Stream and Middle Atlantic Bight shelfbreak front. *JGR*, **121** (8), 6271–6294, doi:
621 10.1002/2016JC011639.
- 622 LaCasce, J., 2008: Statistics from lagrangian observations. *Progress in Oceanography*,
623 **77** (1), 1–29.
- 624 Lilly, J. M., and S. C. Olhede, 2009: Bivariate instantaneous frequency and bandwidth.
625 *IEEE Transactions on Signal Processing*, **58** (2), 591–603.
- 626 Lumpkin, R., A.-M. Treguier, and K. Speer, 2002: Lagrangian eddy scales in the northern
627 atlantic ocean. *Journal of physical oceanography*, **32** (9), 2425–2440.

- 628 Middleton, J. F., 1985: Drifter spectra and diffusivities. *Journal of Marine Research*,
629 **43 (1)**, 37–55.
- 630 Morrow, R., and Coauthors, 2019: Global observations of fine-scale ocean surface topog-
631 raphy with the surface water and ocean topography (swot) mission. *Frontiers in Marine*
632 *Science*, **6**, 232.
- 633 Nelson, A. D., B. K. Arbic, E. D. Zaron, A. C. Savage, J. G. Richman, M. C. Buijsman, and
634 J. F. Shriver, 2019: Toward realistic nonstationarity of semidiurnal baroclinic tides in a
635 hydrodynamic model. *Journal of Geophysical Research: Oceans*, **124 (9)**, 6632–6642.
- 636 Ponte, A. L., and P. Klein, 2015: Incoherent signature of internal tides on sea level in
637 idealized numerical simulations. *Geophysical Research Letters*, **42 (5)**, 1520–1526.
- 638 Ponte, A. L., P. Klein, M. Dunphy, and S. Le Gentil, 2017: Low-mode internal tides and
639 balanced dynamics disentanglement in altimetric observations: Synergy with surface
640 density observations. *Journal of Geophysical Research: Oceans*, **122 (3)**, 2143–2155.
- 641 Pope, S. B., 2015: *Turbulent Flows*. Cambridge Univ. Press, 771 pp.
- 642 Ray, R. D., and E. D. Zaron, 2016: M2 internal tides and their observed wavenumber
643 spectra from satellite altimetry. *Journal of Physical Oceanography*, **46 (1)**, 3–22.
- 644 Savage, A., and Coauthors, 2020: Low-mode internal tides and small scale surface
645 dynamics in the swot cal/val region. *Ocean Sciences Meeting 2020*, AGU.
- 646 Savva, M. A., and J. Vanneste, 2018: Scattering of internal tides by barotropic quasi-
647 geostrophic flows. *Journal of Fluid Mechanics*, **856**, 504–530.
- 648 Sykulski, A. M., S. C. Olhede, A. P. Guillaumin, J. M. Lilly, and J. J. Early, 2019: The
649 debiased Whittle likelihood. *Biometrika*, **106 (2)**, 251–266, doi:10.1093/biomet/asy071,
650 URL <https://doi.org/10.1093/biomet/asy071>.

- 651 Sykulski, A. M., S. C. Olhede, J. M. Lilly, and E. Danioux, 2016: Lagrangian time series
652 models for ocean surface drifter trajectories. *Journal of the Royal Statistical Society:
653 Series C (Applied Statistics)*, **65 (1)**, 29–50.
- 654 Veneziani, M., A. Griffa, A. M. Reynolds, and A. J. Mariano, 2004: Oceanic turbulence
655 and stochastic models from subsurface lagrangian data for the northwest atlantic ocean.
656 *Journal of physical oceanography*, **34 (8)**, 1884–1906.
- 657 Wagner, G., and W. Young, 2015: Available potential vorticity and wave-averaged quasi-
658 geostrophic flow. *Journal of Fluid Mechanics*, **785**, 401–424.
- 659 Wang, J., L.-L. Fu, H. S. Torres, S. Chen, B. Qiu, and D. Menemenlis, 2019: On the
660 spatial scales to be resolved by the surface water and ocean topography ka-band radar
661 interferometer. *Journal of Atmospheric and Oceanic Technology*, **36 (1)**, 87–99.
- 662 Whalen, C. B., C. de Lavergne, A. C. N. Garabato, J. M. Klymak, J. A. Mackinnon, and
663 K. L. Sheen, 2020: Internal wave-driven mixing: governing processes and consequences
664 for climate. *Nature Reviews Earth & Environment*, **1 (11)**, 606–621.
- 665 Yu, X., A. L. Ponte, S. Elipot, D. Menemenlis, E. Zaron, and R. Abernathey, 2019: Surface
666 kinetic energy distributions in the global oceans from a high-resolution numerical model
667 and surface drifter observations. *Geophys. Res. Lett.*
- 668 Zaron, E. D., 2017: Mapping the nonstationary internal tide with satellite altimetry.
669 *Journal of Geophysical Research: Oceans*, **122 (1)**, 539–554.
- 670 Zaron, E. D., 2019: Baroclinic tidal sea level from exact-repeat mission altimetry. *Journal
671 of Physical Oceanography*, **49 (1)**, 193–210.
- 672 Zaron, E. D., and S. Elipot, 2020: An assessment of global ocean barotropic tide models
673 using geodetic mission altimetry and surface drifters. *Journal of Physical Oceanogra-
674 phy*.

675 Zhao, Z., 2017: Propagation of the Semidiurnal Internal Tide: Phase Velocity Ver-
676 sus Group Velocity. *Geophys. Res. Lett.*, **44** (23), 11,942–11,950, doi:10.1002/
677 2017GL076008.

678 Zhao, Z., M. H. Alford, J. B. Girton, L. Rainville, and H. L. Simmons, 2016: Global ob-
679 servations of open-ocean mode-1 m2 internal tides. *Journal of Physical Oceanography*,
680 **46** (6), 1657–1684.

681 **List of Figures**

682 **Fig. 1.** (a) : Mean field of zonal (blue line), meridional (orange line), total (green) and
683 low-passed (red) velocity amplitudes ; (b) : Zonal velocity at t=750 days (color)
684 with positions of 1/4 of the drifters at the same time represented by black dots.
685 (c) : Averaged temporally low-passed kinetic energy and vertical structure of first
686 baroclinic mode (shifted to be equal to zero at the bottom). 34

687 **Fig. 2.** Trajectories of 3 drifters in three different area of the domain (north (a and b),
688 central (c and d) and south (e and f)) over a period of 40 days and corresponding
689 time series. Left column : Trajectory of each the drifter (black line) with the
690 meridional velocity in the background. The red circle represents the position of the
691 drifter at initial time, t_0 , and the blue diamond the position at mid period. A black
692 straight line is plotted representing a quarter of the wavelength. Right column :
693 Meridional velocity time series along the drifter trajectory in red and at a fixed
694 position (blue diamond in the left figure) in blue. 35

695 **Fig. 3.** Autocorrelation of meridional velocity v computed from Lagrangian outputs (a)
696 and Eulerian one (b). The y-axis corresponds to the y bins in which the autocor-
697 relation have been averaged. The x-axis is the time lag. Horizontal black lines
698 indicate the three latitudes of interest discussed in the paper (see Figs. 2 and 4) 36

699 **Fig. 4.** Autocorrelation of meridional velocity at fixed bin in three different area : north
700 (a and b), center (c and d) and south (e and f) of the domain). The Eulerian (right
701 column) and Lagrangian (left column) autocorrelation derived from our data are
702 represented respectively in blue and red. The autocorrelation corresponding to
703 the best fit of our theoretical model (eq.(10)) with the averaged autocovariance are
704 plotted in black dashed lines. Corresponding values of the fitted parameters are
705 indicated in each panel. 37

706 **Fig. 5.** Estimated eulerian (blue lines) and Lagrangian (red lines) incoherence timescale,
707 \tilde{T} (a), decorrelation of the balanced flow, \bar{T} (b) as well as coherence level, α (c)
708 and tidal and balanced components variance, \tilde{V}^2 (d) and \bar{V}^2 (e). The estimates are
709 found by fitting the theoretical model (Eq.(10)) to the autocorrelation of v . Error
710 due to sampling are computed via bootstrap and represented by the gray area. 38

711 **Fig. 6.** Estimated parameters for five simulations. (a) Lagrangian and Eulerian internal
712 tides incoherence timescales, \tilde{T} . (c) and (d) : Internal tide coherence level, α
713 and total tidal variance, \tilde{V}^2 . (b) balanced flow variance, \bar{V}^2 is also represented.
714 Incoherence timescales lower than 1 day and larger than 40 days were not allowed
715 by our fitting procedure. 39

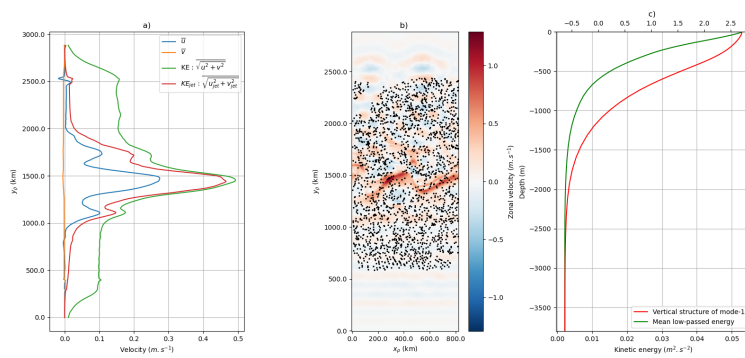
716 **Fig. 7.** Schematics representing synthetic forms of Eulerian (blue lines) and Lagrangian
717 (red lines) autocorrelations depending on the Eulerian coherence level (α) and
718 the ratio of Eulerian incoherence timescale (\tilde{T}_E) over the apparent incoherence
719 timescale (\tilde{T}_{app}). The synthetic cases corresponding to regimes observed in the
720 different part of our domain are numbered as follows: (1) South, (2) center and (3)
721 North 40

722 **Fig. 8.** Envelope of the internal tide autocorrelation functions for 3 simulations (corre-
723 sponding to rows). From top to bottom the balanced flow's strength increases.
724 The envelope of the fitted Eulerian (left column) and Lagrangian (middle column)
725 autocorrelation as well as the predicted Lagrangian autocorrelation (right column)
726 are plotted. 41

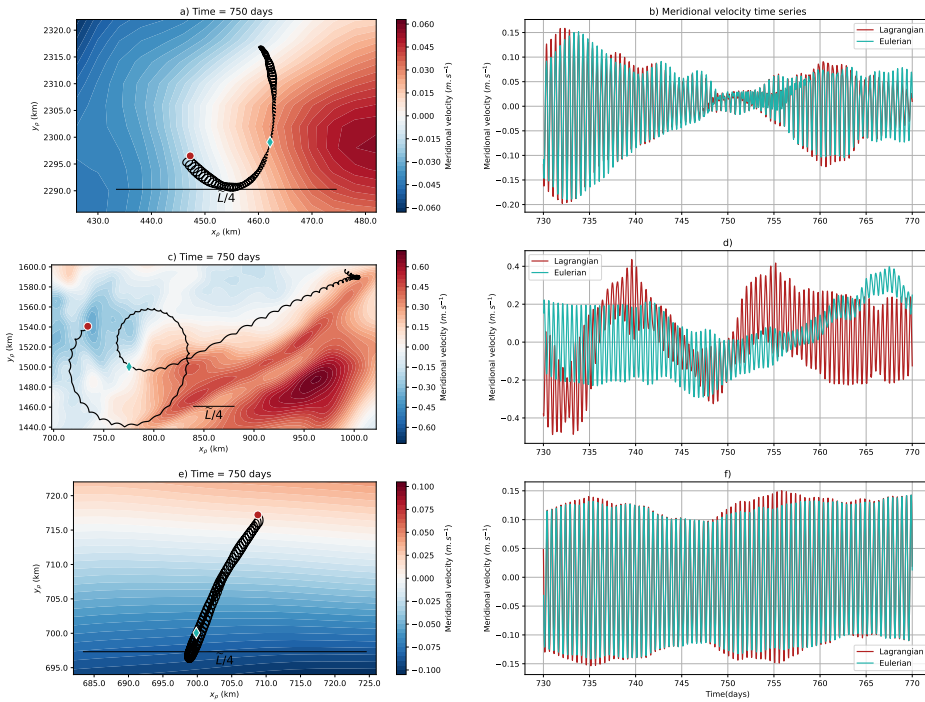
727 **Fig. 9.** (a) Ratio of Eulerian incoherence timescale, \tilde{T}_E , over apparent incoherence
728 timescale, \tilde{T}_{app} , (b) ratio of Lagrangian incoherence timescale, \tilde{T}_L , over apparent

729

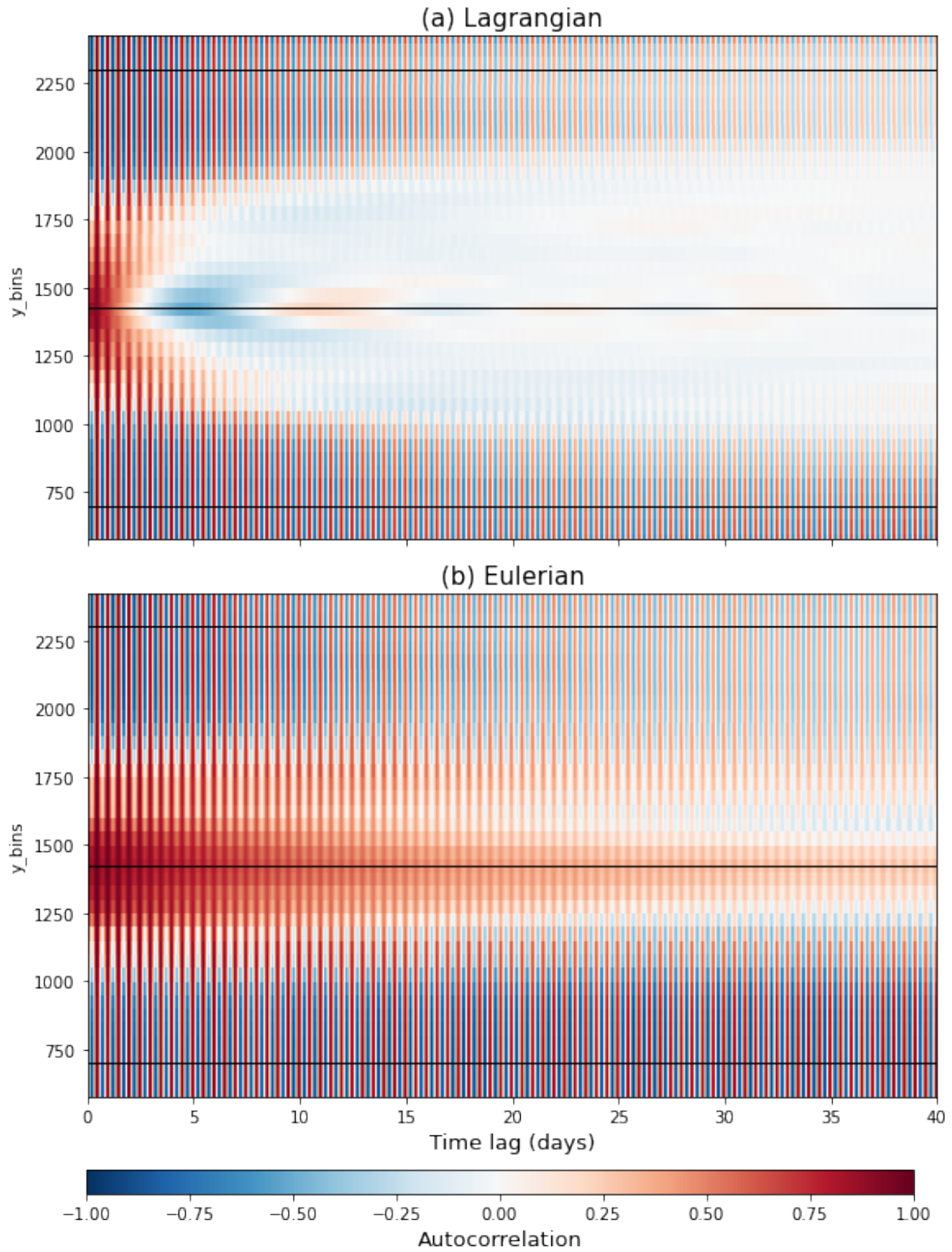
incoherence timescale, \widetilde{T}_{app} and (c) the parameter $k\overline{VT}$ controlling the form of the
730 apparent incoherence autocorrelation (see section 4a) 42



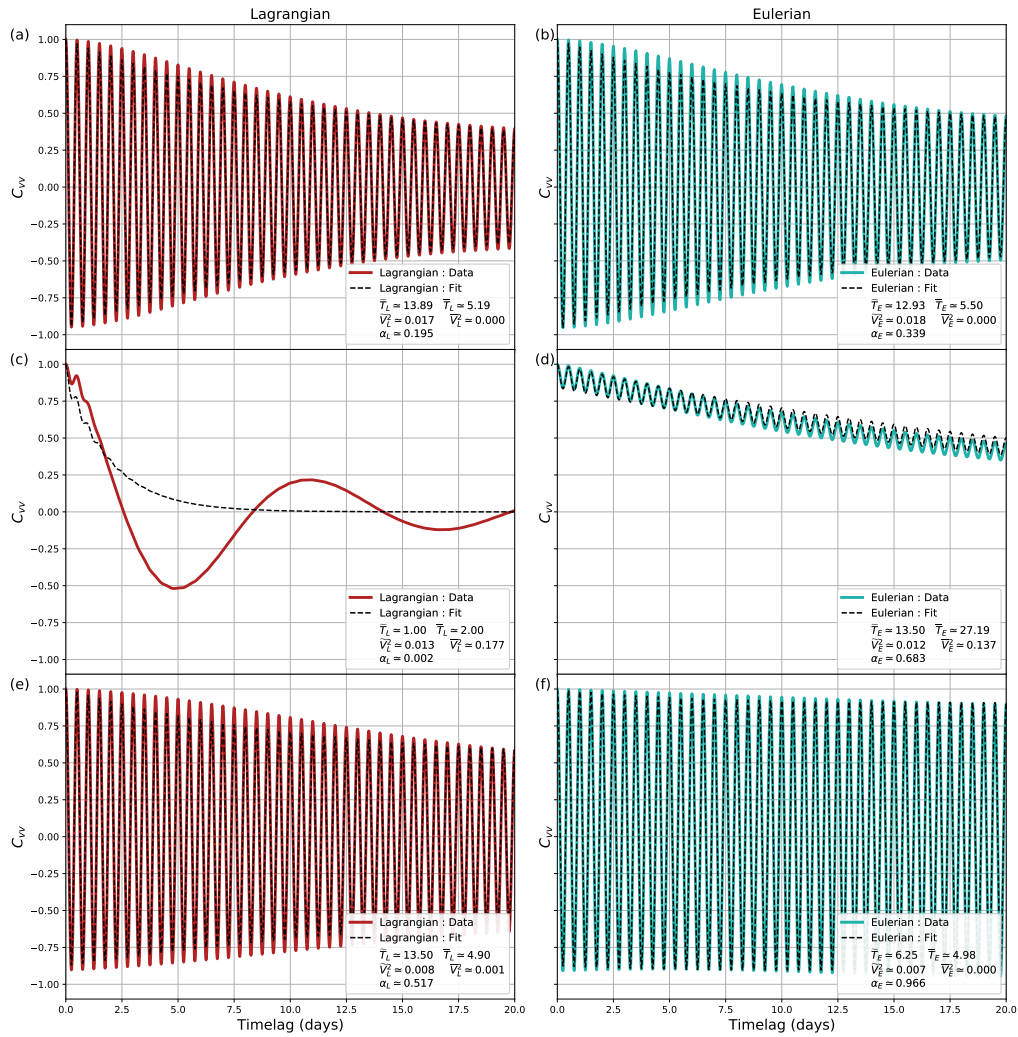
731 Figure 1. (a) : Mean field of zonal (blue line), meridional (orange line), total (green) and low-passed
 732 (red) velocity amplitudes ; (b) : Zonal velocity at $t=750$ days (color) with positions of 1/4 of the drifters
 733 at the same time represented by black dots. (c) : Averaged temporally low-passed kinetic energy and
 734 vertical structure of first baroclinic mode (shifted to be equal to zero at the bottom).



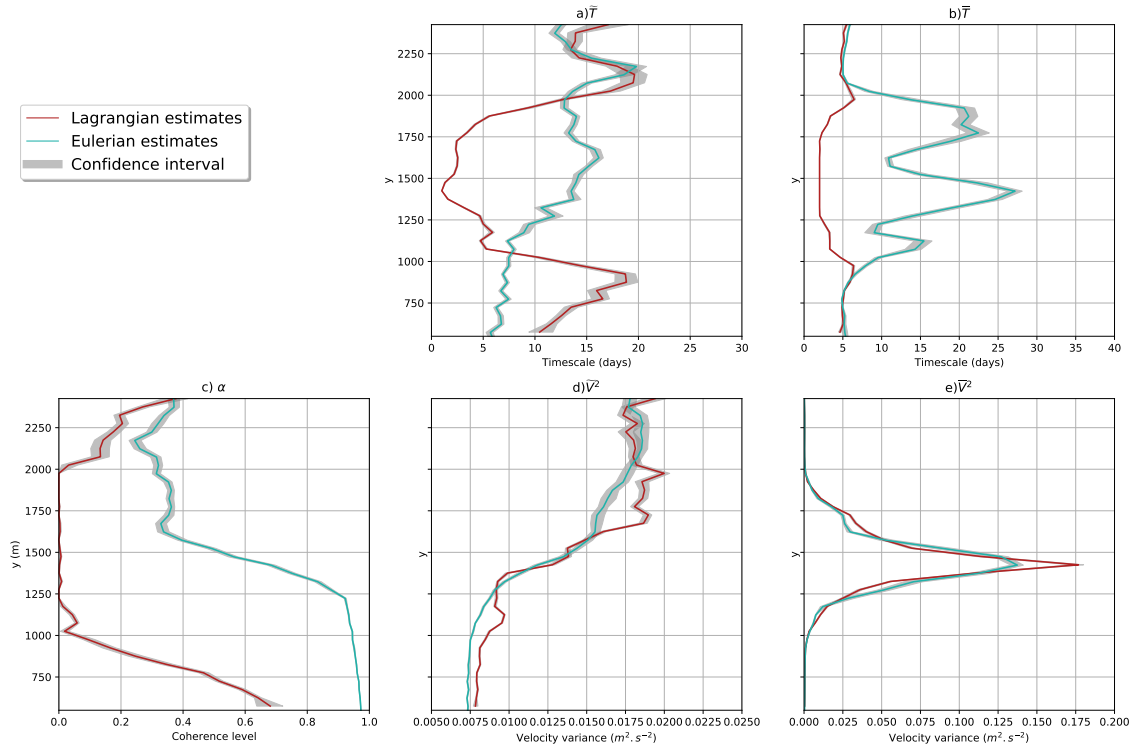
735 Figure 2. Trajectories of 3 drifters in three different area of the domain (north (a and b), central (c
736 and d) and south (e and f)) over a period of 40 days and corresponding time series. Left column :
737 Trajectory of each the drifter (black line) with the meridional velocity in the background. The red circle
738 represents the position of the drifter at initial time, t_0 , and the blue diamond the position at mid period.
739 A black straight line is plotted representing a quarter of the wavelength. Right column : Meridional
740 velocity time series along the drifter trajectory in red and at a fixed position (blue diamond in the left
741 figure) in blue.



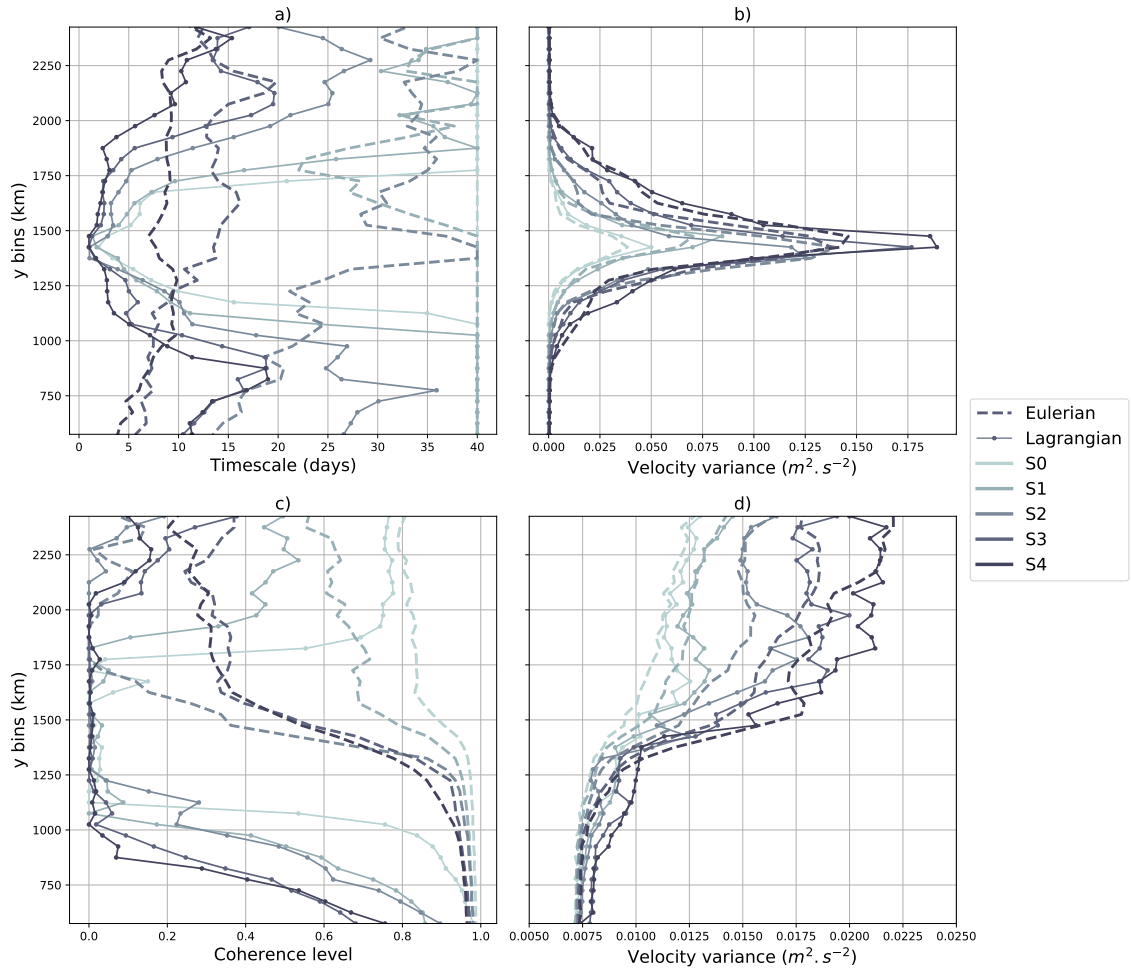
742 Figure 3. Autocorrelation of meridional velocity v computed from Lagrangian outputs (a) and
 743 Eulerian one (b). The y-axis corresponds to the y bins in which the autocorrelation have been averaged.
 744 The x-axis is the time lag. Horizontal black lines indicate the three latitudes of interest discussed in
 745 the paper (see Figs. 2 and 4)



746 Figure 4. Autocorrelation of meridional velocity at fixed bin in three different area : north (a and
 747 b), center (c and d) and south (e and f) of the domain). The Eulerian (right column) and Lagrangian
 748 (left column) autocorrelation derived from our data are represented respectively in blue and red. The
 749 autocorrelation corresponding to the best fit of our theoretical model (eq.(10)) with the averaged
 750 autocovariance are plotted in black dashed lines. Corresponding values of the fitted parameters are
 751 indicated in each panel.



752 Figure 5. Estimated eulerian (blue lines) and Lagrangian (red lines) incoherence timescale, \tilde{T} (a),
 753 decorrelation of the balanced flow, \bar{T} (b) as well as coherence level, α (c) and tidal and balanced
 754 components variance, \tilde{V}^2 (d) and \bar{V}^2 (e). The estimates are found by fitting the theoretical model
 755 (Eq.(10)) to the autocorrelation of v . Error due to sampling are computed via bootstrap and represented
 756 by the gray area.



757 Figure 6. Estimated parameters for five simulations. (a) Lagrangian and Eulerian internal tides
 758 incoherence timescales, \tilde{T} . (c) and (d) : Internal tide coherence level, α and total tidal variance, \tilde{V}^2 .
 759 (b) balanced flow variance, \bar{V}^2 is also represented. Incoherence timescales lower than 1 day and larger
 760 than 40 days were not allowed by our fitting procedure.

761 Figure 7. Schematics representing synthetic forms of Eulerian (blue lines) and Lagrangian (red lines)
762 autocorrelations depending on the Eulerian coherence level (and the ratio of Eulerian incoherence
763 timescale τ_E) over the apparent incoherence timescale τ_{app}). The synthetic cases corresponding to
764 regimes observed in the different part of our domain are numbered as follows: (1) South, (2) center
765 and (3) North